Nanoscale Advances

ROYAL SOCIETY OF CHEMISTRY

PAPER

View Article Online
View Journal | View Issue

Cite this: *Nanoscale Adv.*, 2024, **6**, 606

Controllable synthesis of layered double hydroxide nanosheets to build organic inhibitor-loaded nanocontainers for enhanced corrosion protection of carbon steel†

Minh Vuong Phan, *[ac] Thi Kim Thoa Tran,[ac] Quynh Nhu Pham,[a] Manh Huy Do,[a] Thi Hong No Nguyen,[ac] Minh Ty Nguyen,[a] Thanh Thao Phan[ac] and Thi Xuan Hang To[bc]

The development of layered double hydroxide (LDH) nanosheets as nanocontainers has been intensively studied in recent years. Despite their potential for application on a large scale, their synthesis in an aqueous medium is rarely reported. Herein, we report a straightforward approach for the controllable synthesis of uniform MgAl-LDH nanosheets by an aqueous nucleation process followed by a hydrothermal treatment. The key to this method relies on the well-dispersed LDH nuclei that are produced by high-speed homogenization. Following the nucleation step, the coalescence of the aggregate hydroxide layers is diminished by hydraulic shear forces, leading to the disaggregation and even distribution of LDH nuclei. As a result, the oriented growth of individual crystals along the horizontal plane becomes predominant, leading to a high surface charge density of the hydroxide sheets and preventing their stacking. The electron microscope virtual proofs showed that the particles had a well-defined circular shape with a thickness of about 2–3 nm. Afterward, for the first time, LDH nanosheets were used to prepare LDH nanocontainers loaded with 2-benzothiazolythio-succinic acid (BTSA) by anion exchange. The incorporation of BTSA into the interlayer region and the emission behavior of the inhibitor were investigated. These results indicate that the prepared nanosheets can be utilized as effective nanocontainers for organic inhibitor loading and anti-corrosion application.

Received 28th July 2023
Accepted 18th December 2023

DOI: 10.1039/d3na00570d

rsc.li/nanoscale-advances

1. Introduction

Layered double hydroxides (LDHs), also known as hydrotalcite-like compounds, have been widely studied due to their lamellar structure and anion exchange properties, which make them highly versatile for various applications.[1–3] Their structure includes the positive charge of hydroxide layers formed by the hydroxide of divalent and trivalent cations and the negative charge of counter anions, which neutralize the total charge of LDHs and permit the hydroxide layers to stack on top of each other by electrostatic forces.[4,5] LDHs are represented by the formula $[M_{1-x}^{2+}M_x^{3+}(OH)_2](A^{n-})_{x/n}\cdot yH_2O$, where M^{2+} is a divalent metal cation (Mg^{2+}, Zn^{2+}, Ca^{2+}, *etc.*), M^{3+} is a trivalent metal cation (Al^{3+}, Fe^{3+}, Cr^{3+}, *etc.*) in the hydroxide layers, x is the molar ratio of $M^{3+}:(M^{2+}+M^{3+})$, which typically varies in the range from 0.2 to 0.33 for pure LDHs, and (A^{n-}) represents the interlayer anion.[6–8] The interlayer region can be utilized as a nanospace, wherein anions of various functions are stored and exchanged. Such a property is attributed to extensive research conducted with respect to their potential applications in such a wide range of fields as catalysts, absorbents, flame retardants, polymer additives, and anti-corrosion agents.[9–13] However, the natural aggregation of the lamellar LDH sheets restricts access to the interlayer region, resulting in a decrease in ion exchange capacity, which severely limits their application and overall performance.[2,14] To address this issue, the exfoliation of LDH into nanosheets was proposed.

Nanosheets, which typically range from 0.5 to 3 nm in thickness, are highly anisotropic materials.[15,16] Their unique structure and performance are the attributes that drive the construction of functional blocks for a wide variety of applications.[17–20] In general, LDH nanosheets are typically synthesized *via* two ways: delamination of pristine LDH and direct synthesis *via* the co-precipitation process. The former requires two important factors: (i) organic anion-intercalated molecules that can weaken the interaction between LDH

[a]*Institute of Chemical Technology, Vietnam Academy of Science and Technology, Ho Chi Minh City 700000, Vietnam. E-mail: pmvuong@ict.vast.vn; Tel: +84909312860*
[b]*Institute for Tropical Technology, Vietnam Academy of Science and Technology, Hanoi 100000, Vietnam*
[c]*Graduate University of Science and Technology, Vietnam Academy of Science and Technology, Hanoi 100000, Vietnam*

† Electronic supplementary information (ESI) available. See DOI: https://doi.org/10.1039/d3na00570d

sheets and (ii) polar dispersant solvents that can form hydrogen bonds with the LDH galleries, allowing a large number of solvent molecules to enter the interlayer space and thereby accelerating the delamination process.[18,21–23] Recently, Lian Ma *et al.* have reported a method for fabricating novel nanocontainers by exfoliating MgAl-LDHs into nanosheets and then recombining them with organic inhibitors. The resulting LDH-AIA^- demonstrated itself as a very good inhibitor with regard to copper electrodes.[24] However, the delamination method involves a complex stage that includes the synthesis of LDH pristine and, subsequently, exfoliation. Due to the strong electrostatic interaction between the sheets, LDH was exfoliated in a formamide solution rather than an aqueous medium, which has detrimental environmental effects.[25] The direct synthesis methods of LDH nanosheets relied on controlling the nucleation and growth conditions of LDH nuclei during the co-precipitation procedure.[18,21,26] The key to the approaches is the use of certain reactants, such as hydrogen peroxide or formamide, which can be placed in the LDH galleries to prevent the stacking of hydroxide layers or inhibit the growth of LDH along the *Z*-direction.[2,27,28] Ang Liu *et al.* reported the direct synthesis of ZnAl-LDH nanosheets by co-precipitation in a formamide/water mixture solution followed by an aging step. Then, the LDH nanosheets were applied in the fabrication of highly ordered hybrid polyvinyl butyral/LDH films, which were used as barrier coatings for steel electrodes. The results indicated that the well-oriented LDH nanosheets in the hybrid film significantly improved the corrosion protection of mild steels.[20] Nevertheless, the as-prepared LDH nanosheets need to be dispersed in formamide to prevent re-stacking, which further restricts their practical application.

Even though direct synthesis in an aqueous medium is an attractive route due to the limited use of toxic chemicals and the potential for large-scale synthesis, systematic studies in this direction are still rare. Li *et al.* reported the successful synthesis of LDH nanosheets by the use of excess amounts of lactate in the fast co-precipitation.[29] Subsequently, LDH precursors were sonicated and allowed to stand overnight. This made them disaggregated, producing LDH nanosheets. However, the LDH precursors were not separated from their mother liquor before ultrasonic treatment. This promotes the disorderly growth of LDH nuclei, which affects the final particle size and distribution of LDH particles. Much recently, Quin *et al.* have reported the use of large molecules such as styrene-maleic anhydride (SMA) copolymers, which adhere to the surface of hydroxide layers and weaken the interaction among hydroxide sheets.[30] This caused LDH sheets to grow laterally without stacking during the subsequent aging step. However, the controlled lateral size of the nanosheets was not discussed. To the best of our knowledge, the effect of the LDH nuclei dispersion on the tunable particle size of LDH nanosheets is not fully understood. Moreover, the use of LDH nanosheets to construct organic inhibitor-loaded nanocontainers *via* anion exchange has not been reported previously.

In this study, we propose a straightforward technique for the controllable synthesis of LDH nanosheets in an aqueous medium. This novel approach involved using a high-speed homogenizer to generate evenly dispersed LDH nuclei, which facilitated the growth of nanosheets with uniform particle sizes. In addition, the particle size of LDH nanosheets can be easily manipulated by adjusting the hydrothermal temperatures. Without the use of any organic solvents or hazardous chemicals or the need to operate under N_2 pressure, this approach is simpler and more effective than the current techniques. Then, for the first time, anion exchange was performed on the as-prepared LDH nanosheets to construct a nanocontainer loaded with organic inhibitor anions (BTSA). The anion exchange capacity of the LDH nanosheets and the release behaviors of LDH-BTSA nanocontainers were investigated by various analytic techniques. Finally, the inhibitor efficiency of LDH-BTSA in a NaCl solution was investigated using polarization curves and impedance techniques.

2. Materials and method

2.1. Materials

Magnesium chloride hexahydrate ($MgCl_2 \cdot 6H_2O$, 98%), aluminum chloride hexahydrate ($AlCl_3 \cdot 6H_2O$, 99%), and sodium chloride (NaCl 99%) were obtained from Alfa Aesar. Sodium hydroxide (NaOH, 98%), hydrochloric acid (HCl, 36.5%), and lactic acid ($C_3H_6O_3$, 88%) were purchased from Scharlau. Organic inhibitor 2-benzothiazolythio-succinic acid (BTSA 98.5%) was received from Zhengzhou HQ Material Company. All the chemicals were used as received.

The S45C carbon steel electrodes with a surface area of 1.13 cm^2 were used to prepare the working electrode. For all experiments, the electrode surface was polished with SiC abrasive paper (Fujistar-Japan) from 300 to 1200 grades, rinsed with ethanol, and dried before testing. The surface compositions of electrodes after polishing were 3.14 wt% C, 0.98 wt% O, 0.08 wt% Si, 0.78 wt% Mn, 1.28 wt% S, 0.05 wt% P, 0.18 wt% Cr, 0.09 wt% Ni and the rest is Fe.

2.2. Preparation of ultrathin nanocontainers

2.2.1. Preparation of LDH nanosheets. The ultrathin LDH nanosheets were directly synthesized by a co-precipitation method in conjunction with homogenization treatment, followed by an aging step that was carried out under conditions of continuous stirring. In brief, a 2.4 M NaOH solution was added dropwise to a 200 mL salt solution consisting 0.5 M $MgCl_2$, 0.25 M $AlCl_3$, and 0.5 M sodium lactate to control the pH of the co-precipitation medium at 10. The as-prepared precipitate (LDH-Cl-P) was collected by centrifuging, washed twice, and re-dispersed into 300 mL of deionized water using a high-speed homogenizer (IKA Ultra-Turrax T25) at 18 000 rpm for 15 minutes to obtain a homogeneous suspension (so-called LDH precursors) denoted as LDH-Cl-H. The obtained suspension was transferred into a 500 mL autoclave and heated to 125 °C at a stirring speed of 250 rpm for 24 h. After cooling to room temperature, the LDH nanosheets were collected by centrifugation at 15 000 rpm and signed as LDH-Cl. A part of the nanosheets were vacuum dried at 80 °C for 12 h in order to determine their characteristics, while the rest were re-dispersed

into DI water for loading the inhibitor. To precisely tailor the particle size of LDH nanosheets, the hydrothermal temperature was adjusted at 80, 100, 125, and 150 °C.

2.2.2. Incorporation of BTSA into LDH nanosheets. The synthesis of LDH-BTSA was performed by an anion exchange method utilizing an LDH-Cl nanosheet. This approach prevents the formation of unwanted products from the reaction of Mg or Al cations with the inhibitor and the precipitation of the inhibitor during the co-precipitation method due to the low solubility of the inhibitor. The procedure involved slowly adding 60 mL of LDH-Cl suspension (40 g L^{-1}) into a reaction vessel containing 500 mL of ethanol and 20 mL of 0.5 M Na_2(BTSA) (equivalent by NaOH from BTSA) under continuous stirring at 65 °C. An anion exchange capacity investigation was conducted at 1, 4, 8, and 24 h in a nitrogen atmosphere to monitor the progress of the reaction. Following the anion exchange, the product was centrifuged, washed with ethanol, and vacuum dried at 55 °C for 24 h. Subsequently, the resulting precipitate was ground into a fine powder for characterization.

2.3. Analytical characterization

The electron microscopic images of the prepared samples were observed using a TEM (JEOL JEM-2100, Japan), FE-SEM (HITACHI SU-8010, Japan), and AFM (Omega scope, Horiba, France). The LDH-Cl suspension was dispersed in ethanol, followed by ultrasonic treatment, and then dropped and dried onto a copper grid for TEM observation or a silicon wafer for FE-SEM and AFM analysis. The crystal characteristics of the LDH colloidal suspensions and dried powders were determined using a Bruker D8 X-ray instrument (Germany), in the range of 2θ 2–80° with CuK_α radiation ($\lambda = 1.5418$ Å). Fourier transform infrared spectra were obtained by FTIR spectroscopy in the range of 400–4000 cm^{-1} using a Tensor 27 spectrometer of Bruker (Germany). Thermogravimetric (TG) analyses of the samples were performed using TA-55 equipment (USA) in temperature range of 30–800 °C at a heating rate of 10 °C min^{-1} under a N_2 stream. Elemental compositions of LDH-Cl and LDH-BTSA were determined by EDS analysis.

The amounts of BTSA intercalated to an LDH interlayer and the released fraction of BTSA in a NaCl solution were analyzed by V-630 UV-vis spectroscopy (Japan). The standard curve was performed at different concentrations: 1, 5, 10, 20, and 50 mg L^{-1} of BTSA in ethanol at 280 nm. For determining the content of BTSA, 10 mg LDH-BTSA was dissolved in 1 mL of 3 M HNO_3 with a sonicator for 5 minutes to ensure the dissolution of the nanocontainer. The resulting solution is filled to 10 mL with absolute ethanol in a volumetric flask and quantitated by UV spectroscopy. The fraction releases of BTSA in a NaCl solution were determined as follows: 300 mg of the nanocontainers were dispersed in 100 mL of different concentrations (0.05, 0.1, and 0.5 M) of NaCl solution at a stirring rate of 300 rpm. At the time of the survey, 1 mL of release solution was collected by a 0.45 μm filter, up to 10 mL in a volumetric flask with ethanol, and also quantitated using a UV spectrometer.

The inhibitory effect of LDH nanocontainers was analyzed by electrochemical measurements performed using a VSP potentiostat from Biologic (France). The setup consisted of a three-electrode cell with an Ag/AgCl electrode as the reference electrode, a platinum grid as the counter electrode, and a bare steel rod as the working electrode. Polarization curves were obtained after immersing the steel rod in 0.1 M NaCl solution for 2 h, with and without LDH at a concentration of 3 g L^{-1}, using a fixed scan rate of 1 mV s^{-1} starting from the open circuit potential. Electrochemical impedance spectroscopy was conducted with a sinus amplitude voltage fixed at 5 mV, ranging from 100 kHz to 10 mHz. The impedance data were collected after 2, 4, 8, and 24 h of immersion. The parameters of impedance diagrams were extracted using Z-fit functions of the EC-Lab (v11.43) software. For comparison, 0.005 M Na_2(BTSA) solution in NaCl 0.1 M was also used for testing. The electrode surfaces and their compositions were also observed using a JEOL JSM-IT200 associated with an EDS detector (Japan).

3. Results and discussion

3.1. Preparation of ultrathin LDH nanosheets

In this study, a high-speed homogenizer was applied to disperse the LDH precursors that were collected from the traditional co-precipitation process, followed by hydrothermal treatment to form a well-defined shape of LDH nanosheets. The schematic illustration of the formation process of the LDH nanosheets is displayed in Fig. 1. At first, a certain amount of lactate was introduced to the co-precipitation process. Lactate molecules can interact with the LDH host surface due to the formation of hydrogen bonds with hydroxide layers. Thus, it can compete with intercalated anions on the surface of the LDH host, leading to a decrease in the stacking of hydroxide layers.[29] However, the use of an excessive amount of lactate can result in the attraction of CO_2 from the air to the synthesis medium.[31] To avoid the penetration of CO_2, a low molar ratio of lactate/Al of about 2/1 was used. In addition, the formation of LDH crystallites theoretically involves two stages: nucleation and aging. There are several distinct processes involved in the growth of LDH nuclei in the mother liquor, including crystal growth, agglomeration, and Ostwald ripening. Therefore, it is difficult to regulate the particle size and distribution of LDH particles without separation from the starting medium.[32,33] In this point of view, in the next step, the LDH precursors were separated from the nucleation medium in order to remove the extra salts that can affect the final particle size of LDHs. After that, the LDH precursors were treated by high-speed homogenization followed by hydrothermal treatment to obtain LDH nanosheets.

The morphologies of the LDH nanosheets obtained from the hydrothermal treatment at 125 °C are displayed in Fig. 2. The FE-SEM images (Fig. 2A and B) revealed that LDH has uniform particles, centered around 143.7 nm and well distributed in the range of 100–200 nm (as shown in Fig. 2F). The TEM image (Fig. 2C) demonstrated that the LDH nanosheets have the morphology of circular nanoplates with a very faint contrast, which is consistent with the ultrathin LDH sheet-like particles. In conjunction with the height profile of LDH nanosheets, the AFM results (Fig. 2D) indicated that the thickness of the nanosheets can reach 1.42 nm, but mostly sheets with

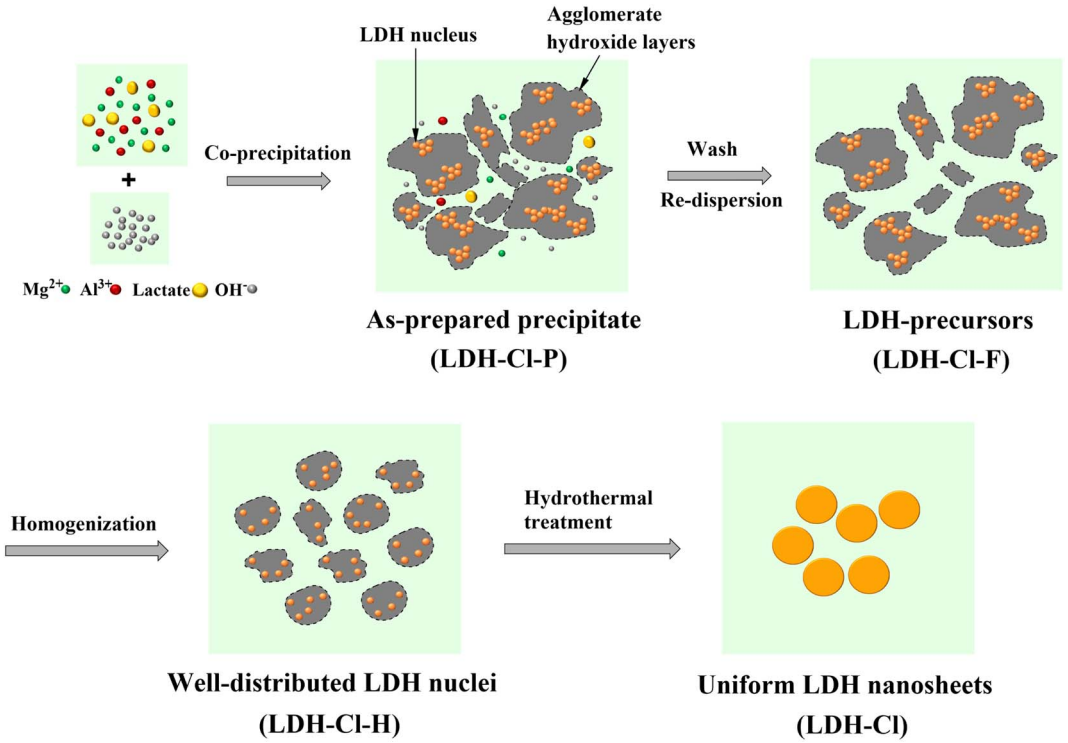

Fig. 1 Schematic illustration of the LDH nanosheet formation process.

a thickness of 2–3 nm were observed (Fig. 2E). Thicker plates (brighter particles on the AFM image) were observed, which may be due to the accumulation of numerous LDH platelets after sample drying, as also confirmed by FE-SEM observation (see Fig. 2B). In addition, the LDH suspension exhibited the Tyndall effect when the laser beam was incident from the side (the insert image of Fig. 2C). This indicated that the LDH nanosheets were dispersed uniformly.

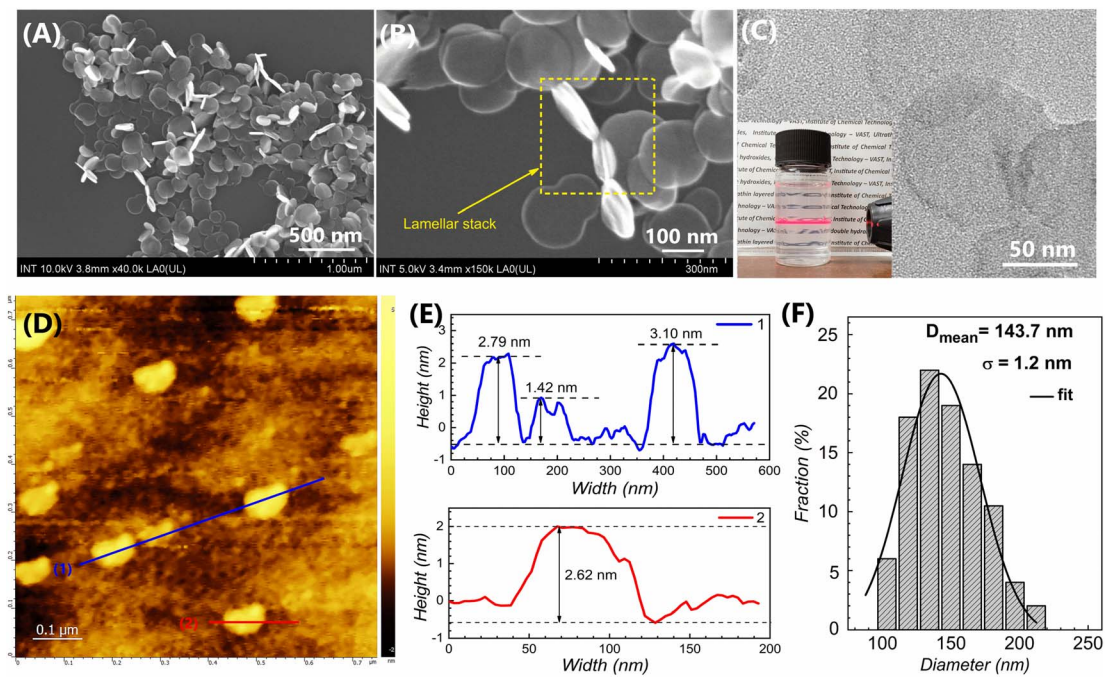

Fig. 2 Virtual microscopic images: FE-SEM (A and B), TEM (C), AFM (D) and height profiles (E) of LDH-Cl nanosheets and size distribution graph (F) obtained from the FE-SEM image (A). The inset image of (C) is a photograph of LDH-Cl nanosheets in an aqueous suspension with the Tyndall effect.

In order to further tailor the particle size of the LDH nanosheets, the hydrothermal treatment temperatures were varied. Fig. 3A depicts the particle hydrodynamic size distribution of nanosheet samples. According to the DLS results, all of the LDH-Cl samples exhibited a narrow distribution and a low PI index of about 0.1–0.2 (Table S1†), indicating homogeneous dispersion in water. The average diameter of LDH-Cl increased from 77.4 to 115.4, 168.4, and 212.5, corresponding with the increase in temperature from 80 to 100, 125, and 150 °C, respectively. Compared to the LDH-Cl sample hydrothermally treated at 125 °C, the other samples showed the same morphology of a circular nanoplate (Fig. S1†). The hydrodynamic size measured by the DLS method is in good agreement with the particle size that was observed from the FE-SEM analysis. Additionally, the extremely high zeta potential, greater than +60 mV (Table S1†), indicated that the final homogeneous suspensions were stable.

3.2. Nanosheet formation mechanism

To clarify the homogenization treatment's effect on the size distribution of LDH precursors, we prepared the control sample without the homogenization treatment (denoted as LDH-Cl-F). Fig. 3B and C present the hydrodynamic size distribution of the prepared LDH samples, as determined by DLS measurement, and the results are summarized in Table 1. The LDH-Cl-F suspension displayed a bimodal particle size distribution (Fig. 3B), a high polydispersity index (PI: 0.638), and an average size of about 1819.8 nm. This indicated the high aggregate of nucleation clusters in the freshly precipitated sample. In contrast, the sample LDH-Cl-H showed a good distribution with a lower PI value of 0.349 and a hydrodynamic size of 363.8 nm. Furthermore, the zeta potential of LDH-Cl-H (listed in Table 1) showed a significant increase compared with LDH-Cl-F (+45.1 *vs.* +14.8 mV). These observations suggested that the aggregate LDH precursors were effectively dispersed into a much smaller species, forming a stable system through high-speed homogenization. It should be emphasized that, during the co-precipitation, the nuclei are located within the hydroxide layers, which are aggregated to form an amorphous matrix due to the sharing of surface anions at the edge sites.[33,34] Through evidence from DLS analysis, it was postulated that hydraulic shear forces diminished the coalescence of the aggregate hydroxide layered, leading to the disaggregation and even distribution of LDH nuclei. Subsequently, the hydrothermal treatment was applied to both LDH-Cl-F and LDH-Cl-H samples in order to study the effect of LDH nucleus texture on the particle size and distribution of the resulting products. After hydrothermal treatment, a decrease in particle size was observed in both samples. This can be explained by the conversion of the aggregate precursors into layered structures through diffusion and crystallite ripening.[33,35] The resulting LDH nanosheets (so-called LDH-Cl in Fig. 1) exhibited a well-distributed particle size (Fig. 3C) and a low PI value of 0.180, suggesting homogenously dispersed LDH nanosheets. Nevertheless, the treated LDH-Cl-F sample exhibited a broad distribution curve with a significantly higher PI value of 0.531 and a larger particle size of 245.9 nm, indicating the agglomerate of

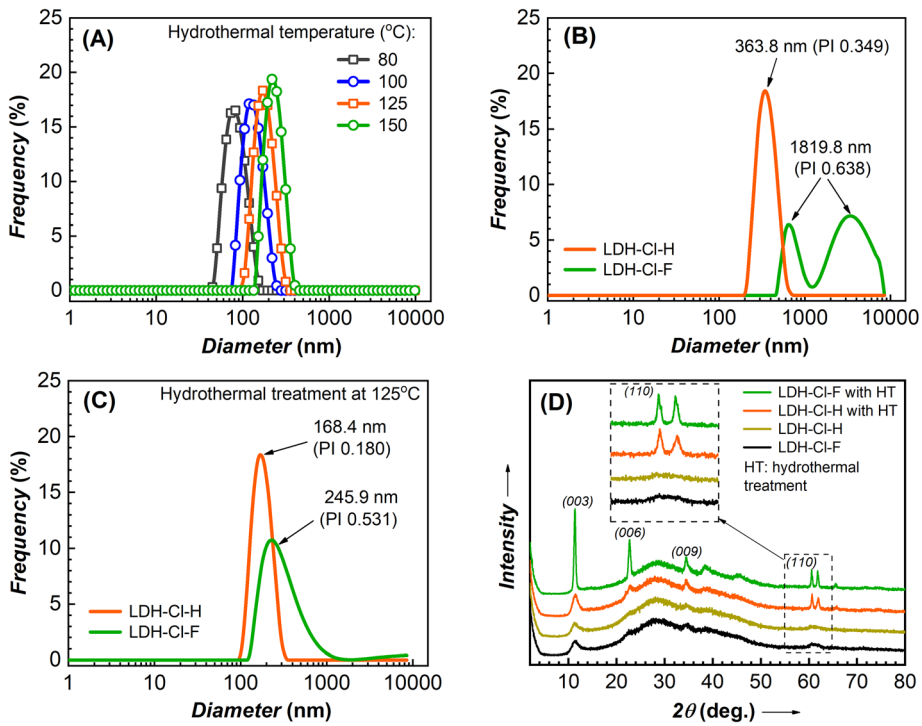

Fig. 3 Particle hydrodynamic size distribution of LDH-Cl nanosheets prepared at various hydrothermal treatment temperatures (A), LDH-Cl-H, and LDH-Cl-F suspensions with (B) and (C) without hydrothermal treatment, and the corresponding XRD patterns (D) of gel-like samples centrifuged from LDH colloidal suspensions.

Table 1 Zeta potential and hydrodynamic size of the LDH-Cl-F and LDH-Cl-H colloidal suspensions before (A) and after (B) hydrothermal treatment at 125 °C

Prepared sample	Hydrothermal temperature (°C)	Zeta potential (mV)	*Z*-Average (nm)	PI value
LDH-Cl-F	—	+14.8	1819.8	0.638
LDH-Cl-H	—	+45.1	363.8	0.349
LDH-Cl-F	125	+35.2	245.9	0.531
LDH-Cl-H	125	+73.9	168.4	0.180

the final product. In addition, the thickness of the obtained LDH plates (approximately 50 nm, as determined by the FE-SEM observation in Fig. S2†) was much larger than that of the LDH-Cl sample. These observations suggested that the even distribution of LDH nuclei promoted the growth of individual crystals but limited the stack of hydroxide sheets, leading to the formation of ultrathin LDH sheets.

The growth of LDH nanosheet crystallites was also determined by XRD analysis (Fig. 3D). The characteristic peak at 2θ: 11.279°, 22.643°, and 34.454° corresponding to the (003), (006), and (009) planes are collectively described at (00*l*) reflections, which is typical for the layered structure of LDH.[36,37] The XRD patterns of the gel-like precipitated samples exhibited broad peaks for LDH-Cl-H and LDH-Cl-F. This suggested that poorly crystalline LDH phases were formed *via* the co-precipitation process and were unaffected by homogenization. Following hydrothermal treatment, the characteristic reflections of the (00*l*) and (110) peaks (at 2θ 61.509°) for LDH-Cl-F increased significantly, indicating the formation of well-crystallized LDHs and the stacking of hydroxide sheets. In contrast, the XRD result of LDH-Cl revealed a slight increase in the reflections of the (00*l*) peaks, but a significant increase in the reflections of the (110) peak, indicating that the growth of LDH sheets along the horizontal plane has more advantages than the growth along the *c*-axis. It could be explained by the high-energy surfaces of the edge sides, which promoted a higher growth rate than low-energy surfaces of the basal plane, leading to a circular shape of LDHs, as observed by the electronic microscope images (Fig. 2(A)–(C)).[34] In addition, the oriented growth of individual crystals leads to the high surface charge, which can be indicated through the high zeta potential (+73.9 mV) and is sufficient to stabilize nanoparticles by electrostatic stabilization. Thus, this characteristic can contribute to preventing the stacking of hydroxide layers on each other during synthesis.

According to these findings, we hypothesized that the key to this approach relies on the well-dispersed LDH nuclei. After the nucleation stage, the amorphous phase of hydroxide layers, which consists of LDH nuclei clusters, was separated from their mother liquor and re-dispersed in water (LDH-Cl-F). Then, the weak interactions between aggregated hydroxide layers can be easily broken under the impact of hydraulic shear forces, leading to evenly dispersed LDH nuclei. The segregated LDH nuclei promoted the growth of individual crystals through the Ostwald ripening, in which the growth in the horizontal plane becomes predominant due to the high-energy surfaces at the edge sides. As a result, the LDH nanosheets are able to resist aggregation by Brownian motion and preserve the stability of the final colloidal suspension. These findings were supported by AFM results (Fig. 2D and E), which indicated that the diameter of LDH sheets (~100 nm) is significantly greater than their thickness (~2–3 nm). It should be noted that the thickness of MgAl hydroxide layer has been investigated in previous research at about 0.477 nm,[7,38] and the basal spacing of LDH-Cl was determined from XRD results to be 0.784 nm. This implies that the prepared nanosheets consist of only a few brucite layers, which revealed the successful synthesis of ultrathin LDHs by a direct synthesis method.

3.3. Organic inhibitor-loaded ultrathin LDHs

The zeta potential of nanosheet colloidal samples collected from hydrothermal reactions at 125 and 150 °C was higher than that of samples treated at lower temperatures (Table S1†). This demonstrated the long-term stability of colloidal nanosheets formed at high temperatures. However, at 150 °C, the reaction pressure was high, exceeding the limit of our autoclave reactor. As a result, to ensure the safety and replication of the experiment, the LDH-Cl hydrothermally treated at 125 °C was chosen as the precursor to conduct the anion exchange reaction. To study the structure of components in an anion exchange reaction, a powder X-ray diffraction was conducted, and the patterns of pristine BTSA and prepared samples are displayed in Fig. 4A. The basal spacing and lattice parameters of LDHs were also determined, and are presented in Table S2.† The comparison of the overall XRD patterns of BTSA with the LDH samples indicated the absence of the characteristic signals of BTSA in the region of LDH basal diffraction. The XRD pattern of LDH-Cl exhibits the well-defined diffraction peaks of the (00*l*) reflections. This demonstrated the stack of nanosheets during the preparation of the dried samples. These results are in good agreement with the literature reports and confirm the formation of the LDH structure.[18,39] After loading the BTSA into the interlayer region, the 2θ angle of the (003) plane of LDH-Cl shifted to a lower position of 2θ, which revealed the increasing interlayer spacing of LDH. Thus, it can be concluded that the inhibitor anion was successfully inserted into the material structure, causing the expansion of the layer spacing. Furthermore, upon comparing the XRD plot of LDH-Cl and LDH-BTSA, it was observed that only the characteristic peaks at the (003) and (006) planes were changed significantly after the interstitial of BTSA anions into the material structure. In contrast, the diffraction positions of the (110) plane were equivalent, so the lattice parameter a is similar (0.3058 *vs.*

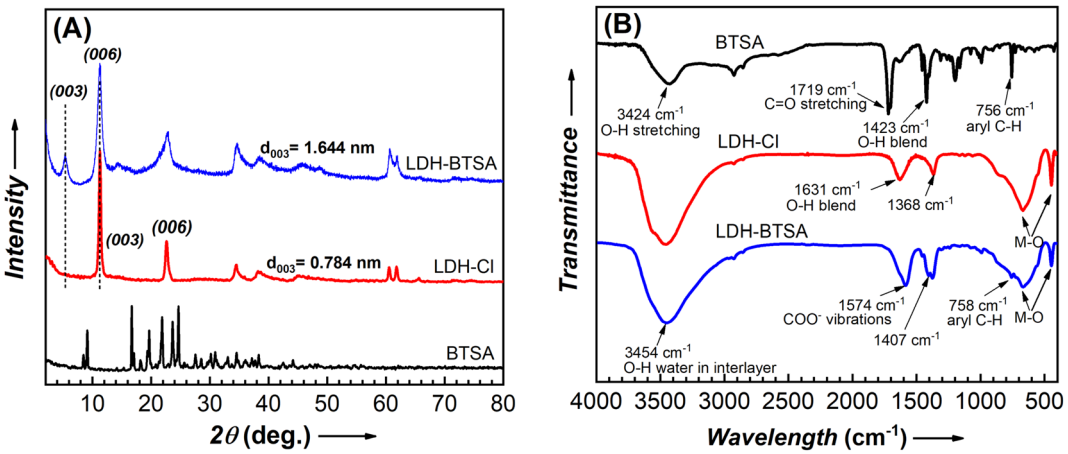

Fig. 4 XRD patterns (A) and FTIR spectra (B) of BTSA, LDH-Cl and LDH-BTSA.

0.3038 nm), suggesting that the lamellar layer has the same chemical composition in both cases.[24] This indicating the anion reaction occurs without a significant defect to the structure of the cation layer. In addition, the reflection peaks of the planes (110) and (113) are broadened, indicating a lower level of crystallinity of LDH-BTSA than that of the LDH precursor. This may attribute to the larger size of the anion interlaced.[40,41]

The presence of BTSA in the structure of the nanocontainers was confirmed using the FTIR spectrum (Fig. 4B). A broad range between 3000 and 3750 cm^{-1} is observed, characterized by the prolonged OH group of hydroxide layer and water blending between 1600 and 1650 cm^{-1} (O–H blending) present on all of the samples.[7,42] LDH-Cl exhibited a well-defined peak at a frequency of 1368 cm^{-1}, which can be attributed to the presence of Cl^- anions in the LDH structure.[39] The weak absorption bands located at 2926 cm^{-1} and 1120 cm^{-1} may correspond to the C–O and C–H stretching of the lactate anion present in LDH-Cl. Additionally, the strong peak at 446 cm^{-1} and the wide peak at 670 cm^{-1} are assigned to the oscillation of Mg–OH and Al–OH of the hydroxide layer.[43] As regards the pure BTSA, the peaks at about 2929 cm^{-1} and 756 cm^{-1} can be assigned to the CH group in the aromatic ring structure. Moreover, the strong peaks at 1719 cm^{-1} and 1423 cm^{-1} can be attributed to the C=O and O–H stretching of the –COOH group.[44] A comparison between LDH-BTSA and pure BTSA spectra revealed the disappearance of the typical peaks of the COOH group at a frequency of 1719 cm^{-1}, and the emergence of new peaks at around 1574 cm^{-1} and 1402 cm^{-1}, which can be attributed to the asymmetric and symmetric vibrations of the COO– groups.[44,45] The band characteristics of metal–O at 447 cm^{-1} and 674 cm^{-1} also remained in the spectrum of LDH-BTSA. Furthermore, the significant change in the intensity and peak position could be indicating the interaction between the organic inhibitor intercalated and the hydroxide layer of LDH.[46] The combined XRD and FTIR results clearly show the successful intercalation of organic inhibitor anions to the interlayer of LDHs.

The thermal properties of LDH and BTSA were also determined by the TGA method and the resulting curves are displayed in Fig. S3.† LDH-Cl and LDH-BTSA show the same amount of water loss (absorbed and interlayer water) of approximately 10 wt% at temperatures below 200 °C. It can be seen that the pure BTSA exhibited significant degradation at about 180–280 °C, while the degradation of BTSA in LDH-BTSA was observed at 380–500 °C. This can be attributed to the lamellar structure's barrier effect, which slowed the diffusion of volatile compounds.[47] Compared to the weight loss results between the two types of LDH, the BTSA content in the interlayer region of the nanocontainer was calculated to be about 36.6%.

3.3. Inhibitor loading capacity of LDH nanosheets

To investigate the loading capacity of LDHs, the resulting LDH-BTSA samples were collected at different times during the anion exchange. The amounts of BTSA (wt%) content in LDH-BTSA at different times of anion exchange were calculated by the UV spectrum, and it is displayed in Fig. 5A (the calibration of pure BTSA was the inset). At the beginning of the anion exchange reaction, the BTSA loaded on LDHs showed a positive correlation with the initial amount of BTSA. After one hour of the experiment, the BTSA weight percentage content was found to be 12.98%. Subsequently, with the increase in reaction time, the BTSA content was dramatically increased to about 37.89% after 24 h. Furthermore, it did not change significantly during the increasing reaction time of 48 h. This result is well matched with the BTSA content determined by the TGA method.

To study the effect of anion exchange time on the nanocontainer structure, XRD analysis was performed on the sample obtained at different times of reactions (Fig. 5B). The results indicate that after one hour of reaction, the typical peak at $2\theta = 5.372°$ due to the diffraction of the (003) plane appeared. Furthermore, at different times, the positions of the diffraction angles at the (00*l*) plane do not change significantly, confirming the stability of the LDH structure during the anion exchange reaction. Although it can be difficult to draw definitive conclusions about the relationship between intensity and amount in XRD, we observed that the area ratio between the diffraction peaks at (003) and (006) increased with the anion exchange

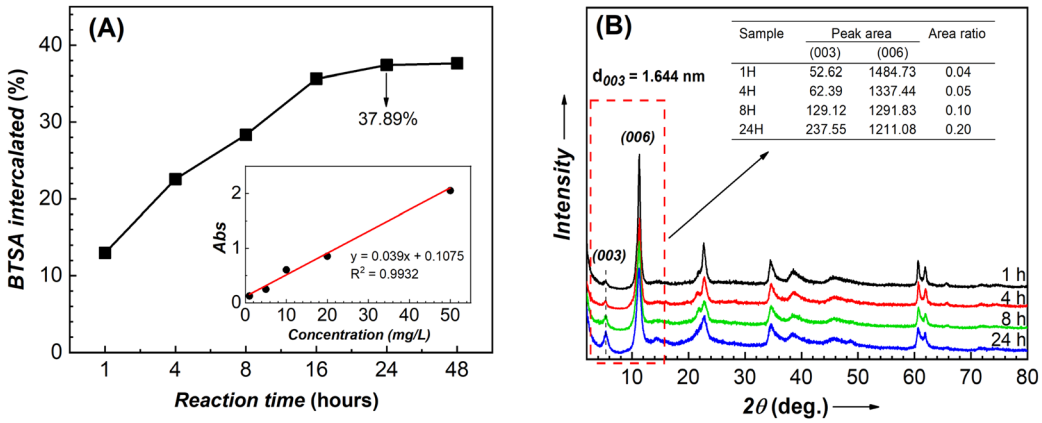

Fig. 5 (A) Inhibitor loading capacity of LDH-Cl nanosheet. (B) XRD patterns of LDH-BTSA at 1, 4, 8, and 24 h of anion exchange. The inset image of (A) is the calibration of pure BTSA in the range of 1–50 mg L^{-1} in ethanol.

time. In particular, the area of the (003) diffraction peak increased, while the (006) diffraction peak decreased. In conjunction with UV analysis results, this suggested that the increasing number of organic ingredients intercalated into the basal spacing can influence the crystallographic structure of LDHs.

In comparison with pristine LDH-Cl, the morphology of LDH-BTSA (as depicted in Fig. 6) maintained uniform particle size with a circular nanoplate shape and did not exhibit significant changes during 24 h of anion exchange. This indicated that the reaction mechanism is topotactic transformation,[40] by the fact that the lateral size and distribution of the nanoplates are crucial factors in taking full advantage of the material. The disorderly growth results in high aggregation, which is the major drawback for the application of LDHs, because it impedes access to the most active sites on the surface of the crystallites, affects the diffusion of anionic species in the interlayer, and reduces the anionic exchange rate.[2,14] Thus, controlling the size distribution of the nanocontainers is important to enhance the performance of the materials.

The element content in the LDH-BTSA product and precursor was determined by EDS analysis and compared in Table 2. The atomic ratios of Mg/Al are close in both cases of LDH (1.99 *vs.* 2.02) and similar to the molar theoretical use at synthesis (2.00). The presence of BTSA in the component of the reaction mixture does not influence the Mg/Al atomic ratio of LDH, and this can be assumed that the anion exchange reaction occurs without any further reaction, which was confirmed in

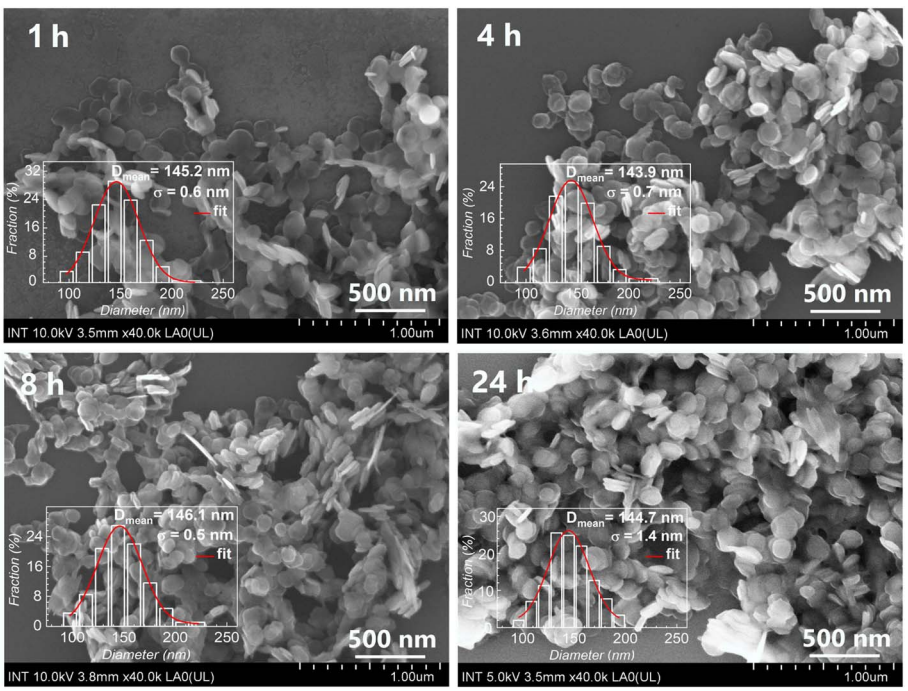

Fig. 6 FE-SEM images of LDH-BTSA at 1, 4, 8, and 24 h of anion exchange.

Table 2 The element composition of LDH-Cl, LDH-BTSA and LDH-BTSA after release in 0.1 M NaCl solution for 24 hours

	Content (wt%)				Molar ratio		
Samples	Mg	Al	S	Cl	Mg : Al	BTSA : Al	BTSA (wt%)
LDH-Cl	20.78 ± 0.16	11.59 ± 0.14	—	11.47 ± 0.14	1.99	—	—
LDH-BTSA	14.73 ± 0.28	8.08 ± 0.23	7.56 ± 0.21	—	2.02	0.787	37.56
LDH-BTSA released	16.34 ± 0.19	9.00 ± 0.15	5.01 ± 0.06	2.07 ± 0.06	2.01	0.468	22.27

XRD analysis. The S content in the LDH-BTSA is 7.56 wt%, while the S content of pristine BTSA determined by EDS is 20.13 wt%. Based on the parameters, the BTSA content in LDH-BTSA was calculated to be 37.56 wt%. This results in good agreement with the TGA and UV analyses. The small distinctions between the results obtained from different methods were insignificant and could be attributed to the specific characteristics of each method. In addition, the absence of chloride anions in the composition of LDH-BTSA indicated the complete replacement of these anions, suggesting the successful accomplishment of the anion exchange process after 24 h of reaction.

3.4. Release of BTSA in a corrosion medium

As an anion exchange compound, the LDH nanocontainer can be exchanged with corrosive anions as chloride and release the organic inhibitor anion, which is the most important factor influencing the efficiency of the corrosive inhibitor.[1,13,46] To understand the kinetics of the release of inhibitors in a corrosive medium, we conducted the anion exchange reaction at different concentrations of NaCl solutions. The amount of BTSA anions was quantified by UV absorption spectra. The released sample displayed an absorption peak at about 280 nm, which corresponds to the characteristic of BTSA (Fig. 7A). A large number of BTSA anions were released that can be observed for the first 8 h (Fig. 7B). After that, the release of BTSA remains significantly lower. After one day of exposure, the fraction of organic release reached 21.96 wt%, 41.77 wt%, and 57.63 wt%, corresponding to 0.05 M, 0.1 M, and 0.5 M of NaCl solution. It can be clearly shown that the amount of BTSA released depends on the NaCl concentration. The higher concentration of the chloride anion can be attributed to the strong electrostatic interaction between the positively charged hydroxide layer and anions, and it becomes easier for them to penetrate and replace

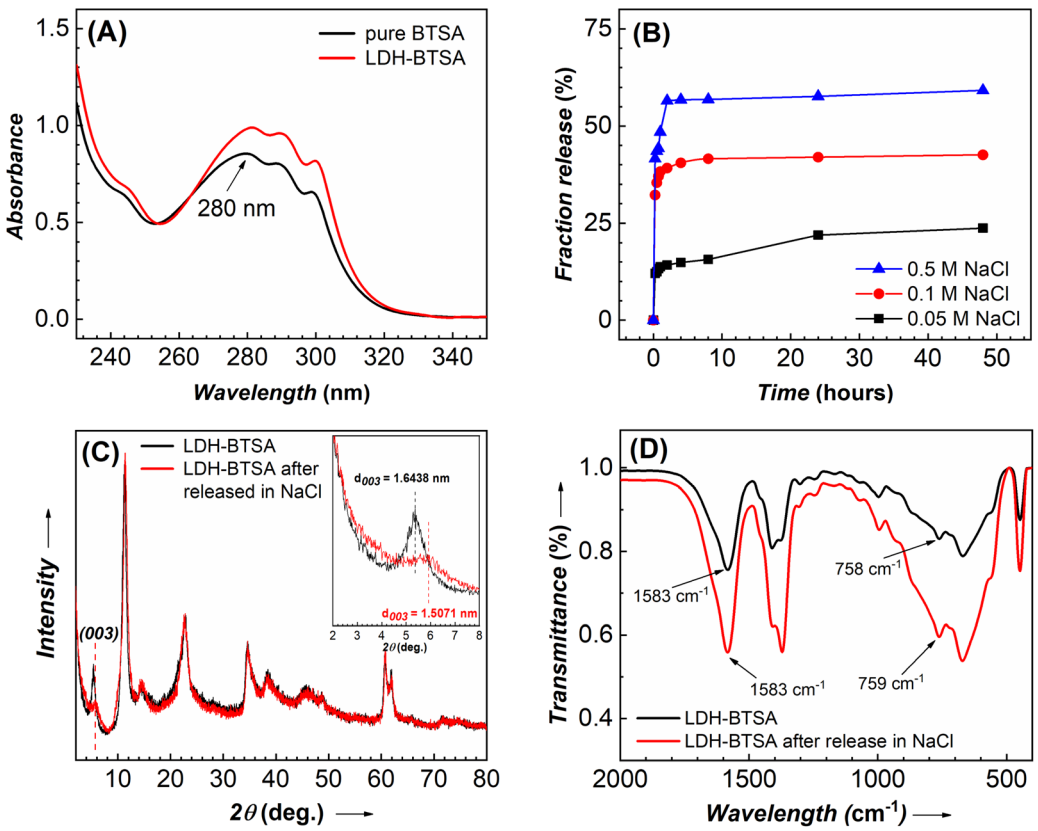

Fig. 7 (A) UV absorption spectra of BTSA and LDH-BTSA after release in 0.1 M NaCl. (B) Fraction release of BTSA at different concentrations of NaCl solutions. (C) XRD and (D) FTIR curves of LDH-BTSA before and after 24 h release in a 0.1 M NaCl solution.

the BTSA anion in interlayers.[48] The EDS results (Table 2) indicate that after release in the NaCl solution, the BTSA anion content in the nanocontainer decreased, accompanied by the appearance of chloride anions. These results confirm the role of the LDH structure in the corrosive medium. It can release the inhibitor and trap the aggressive anion *via* an anion exchange reaction.[46,49]

After 24 h of release in the NaCl solution, the LDH was collected for characterization by XRD (Fig. 7C) and FTIR (Fig. 7D) to study the structure of the nanocontainer after exposure to the corrosive medium. The position of diffraction peaks was similar except for the shift on the (003) plane. The released LDH-BTSA shows a decrease in the basal spacing (from 1.6438 nm to 1.5071 nm). This effect can be explained by the structural arrangement of the anion intercalated in the layer structure. It should be noted that the dimension of the chloride anion is less than that of the BTSA anion. This can cause a decrease in basal spacing after the release of BTSA. Furthermore, a significant decrease in the diffraction peak intensity at the (003) plane was observed. This can be explained by the reduced amount of BTSA in the layer structure of LDHs. Fig. 7D shows the FTIR comparison results of the LDH-BTSA before and after release in NaCl. After exposure to the sodium chloride solution, no significant changes were observed on the FTIR spectrum, suggesting that BTSA is still stored in the nanocontainer and an equilibrium of anion exchange was reached.[46]

3.5. Corrosion inhibitor effect of LDH-BTSA

The inhibitor efficiency of the nanocontainers for carbon steel electrodes was determined by the polarization test. The sample with BTSA anion at a concentration of 0.005 M in a 0.1 M NaCl solution was also conducted for comparison. The results of polarization curves obtained after 2 h of exposure to the corrosive medium are presented in Fig. 8. The corresponding parameters and inhibition efficiency are listed in Table S3.† It can be clearly shown that in the presence of BTSA, the corrosion potential of the samples shifted to a higher positive value and a lower current density than those of the blank solution. This confirmed that BTSA works as an anodic inhibitor. In the case of the presence of LDHs, the deposition of the LDH lamellar structure with a positive electrical charge onto the anodic site of the electrode surfaces also changed the corrosion potential to higher positive values. This change can improve the corrosion inhibitor efficiency.[43,50]

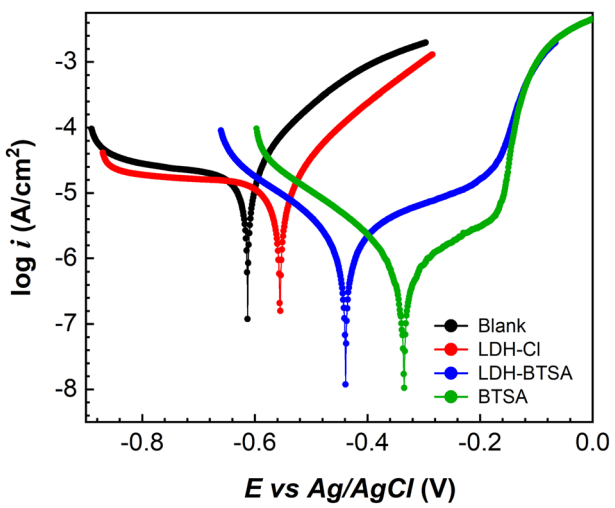

Fig. 8 Polarization curve of steel electrodes after 2 hours of immersion in a 0.1 M NaCl solution without inhibitor and containing 3 g L^{-1} of LDH-Cl, LDH-BTSA, and 0.005 M Na_2BTSA.

The BTSA solution showed the lowest corrosion current density at 0.598 μA cm^{-2}, whereas the blank solution had the highest value of 19.202 μA cm^{-2}. This is probably due to the action of BTSA molecules, which adsorbed onto the oxide layers formed on the metal surface, leading to a reduction in the current density. The presence of BTSA in the LDH structure resulted in a corrosion current density of 1.866 μA cm^{-2}, significantly lower than that of the sample with LDH-Cl at 12.987 μA cm^{-2}. The inhibition efficiencies of LDH-Cl and LDH-BTSA were 32.4% and 90.3%. This significant increase could be explained by the effect of the nanocontainer, which can release organic inhibitors into the corrosive medium. Additionally, the reaction between the organic inhibitor and ferrous ions released from the electrode surface can result in forming barrier films by insoluble products on the substrate surface, which can also contribute to reducing the corrosion rate.[47,51,52]

The inhibition effect of the LDH with the organic inhibitor anion was also investigated by EIS measurements. Nyquist plots and Bode plots of steel electrodes after 2, 4, 8, and 24 h of immersion in 0.1 M NaCl solution are displayed in Fig. 9. In addition, the fitting parameters consisting of R_s, R_p, and R_f represented solution resistance, polarization resistance, and film resistance obtained from the impedance plots of electrodes are also presented in Table S4.† The polarization resistance (R_p) is the main parameter used to estimate the efficiency of inhibitors. The blank and LDH-Cl solutions exhibited a one-time constant; meanwhile, BTSA and LDH-BTSA solutions showed a two-time constant. This revealed the presence of protective films on the steel surface.[47,51]

The electrolyte resistance of testing samples is slightly changed, which could be caused by the presence of different components in the 0.1 M NaCl solution. Without inhibitors, the lowest impedance value was obtained during the test. After 2 h of exposure, the blank solution obtained R_p of 1300 Ω cm^2 and showed a decreasing trend with the continuous immersion for 24 h. This indicates the degradation of the electrode surface and corresponds to the increased corrosion rate. At the beginning of the test, the LDH-Cl shows an R_p value 1571 Ω cm^2, higher than that of the blank solution, which can be explained by the deposition of lamellar structures on the steel surface to form barriers at the defect sites of the electrode. However, R_p not only insignificantly increases in the case of continuous immersion but also reduces to a low value at the end of the test. This is attributed to the low thickness and porous structure of the precipitated layer by the LDH.[53] In other words, LDH-Cl is limited to performing an anion exchange reaction with chloride anions. Thus, they present limited inhibitive behavior.

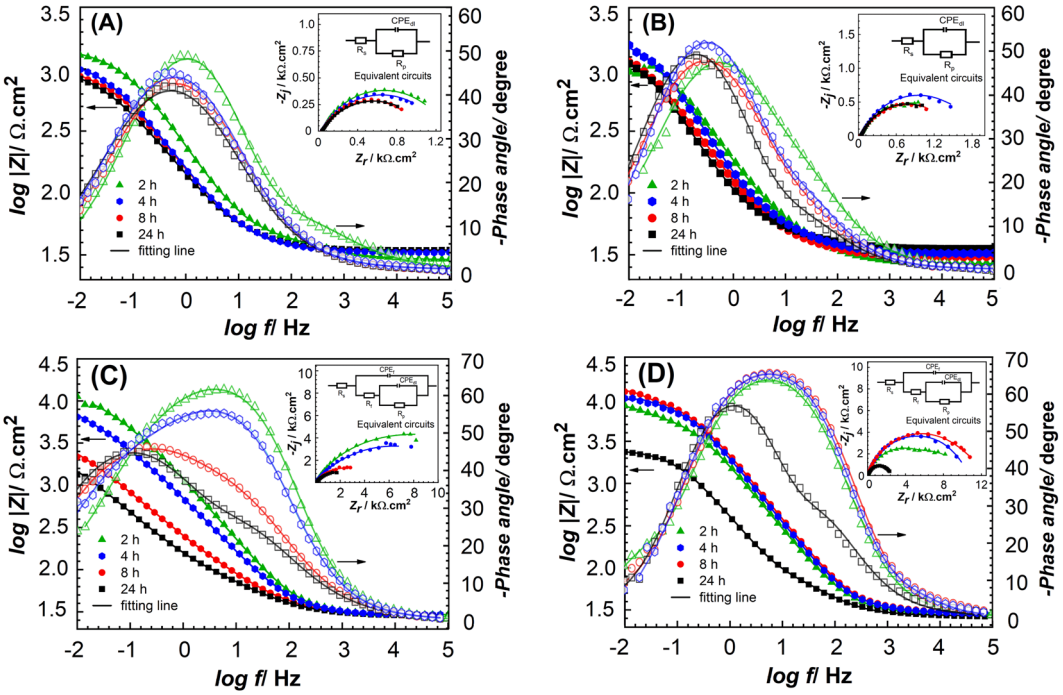

Fig. 9 Bode and Nyquist plots (inset) of bare steel electrodes after 2, 4, 8 and 24 hours of immersion in a 0.1 M NaCl solution without inhibitors (A), with 3 g L^{-1} of LDH-Cl (B), 0.005 M Na_2BTSA (C), and 3 g L^{-1} of LDH-BTSA (D).

The sample testing in the presence of 0.005 M BTSA anion shows the highest R_p value at 14 190 Ω cm^2. Nevertheless, the R_p value showed a significant decrease trend during the increasing time of immersion. In contrast, the samples of LDH-BTSA are associated with different processes. After 2 h of immersion, the LDH-BTSA solution exhibited a high R_p value of 6905 Ω cm^2, suggesting that the intercalated BTSA is highly effective. The R_p value continuously increased to 9703 Ω cm^2 and 11 271 Ω cm^2, corresponding to 4 and 8 h of exposure. This is attributed to the large number of BTSA anions released from the nanocontainer to the corrosive medium, and as a result, the corrosion rate was reduced. This phenomenon indicates the effect of nanocontainers loaded with organic inhibitors with the advantage of the controlled release of organic inhibitors for maintaining the stability of inhibitor efficiency over time. As the immersion time increased to 24 h, the R_p value decreased but remained at a high value of about 3270 Ω cm^2. This can be attributed to the inhibitor molecules being consumed on the metal surface. After 24 h of immersion, the Bode plots showed that the phase angle of LDH-BTSA showed a minimum value of −56°, which was shifted to a higher frequency than that of the other samples. In addition, the two-time constant was exhibited, which revealed the formation of barrier films on the steel surface, which can be used to explain the anodic behavior of the inhibitor.[47,51,54] The R_f value is attributed to the film resistance deposition on the steel electrode surface. With the increasing immersion time, R_f values of the samples with BTSA show a more declining trend than that of the samples with LDH-BTSA. This indicates that the barrier films former by LDH-BTSA are more stable than free BTSA. After 24 h, R_f was determined to be about 94.3 Ω cm^2 and 135.8 Ω cm^2 corresponding to samples of BTSA and LDH-BTSA. The higher R_f value of LDH-BTSA could be explained by the large numbers of nanocontainers deposited on the steel surface.

3.6. Surface analysis

Finally, to clarify the action of LDH-BTSA on the bare steel, the electrode surfaces after 24 h of immersion in a NaCl solution were also analyzed by SEM and EDS. The SEM observations are presented in Fig. S4.† In the absence of an inhibitor, the crystals of corrosion products are clearly observed on the electrode surface (Fig. S4(A) and (B)†). EDS was used to determine the element composition, and the summarized results (Table 3) revealed that iron and oxygen elements were detected on the electrode surface. The Fe and O contents (wt%) on the surface are 69.28 and 28.49%, respectively. Meanwhile, the Fe and O contents on the selected particles are 56.10 and 40.08%, respectively. In this case, the higher content of oxygen revealed the presence of iron oxides. Thus, these results confirmed the formation of iron oxide particles on the steel surface.

Table 3 EDS analysis results of the electrode surface after 24 hours of immersion in 0.1 M NaCl

Samples		Element content (wt%)						
		Fe	O	C	Mg	Al	S	N
Blank	Surface	69.28	28.49	2.23	—	—	—	—
	Particles (1)	56.10	40.08	3.82	—	—	—	—
LDH-BTSA	Surface	43.34	24.41	14.49	8.35	4.15	2.45	1.79
	Particles (2)	17.05	39.57	23.34	7.29	3.52	5.84	2.69

In addition to LDH-BTSA, the substrate's surface was covered by the lamellar structure of LDH, and the corrosion products as iron oxide crystals disappeared (Fig. S4(C) and (D)†). This indicated the efficiency of the anti-corrosion properties of LDH-BTSA. Some elements, such as the fingerprint of the nanocontainer as Mg, Al, and S, were also detected, which further confirms the deposition of the nanocontainers on the surface of the electrode. The element content of Fe, Mg, Al, and S was 43.34%, 8.35%, 4.15%, and 2.45%, respectively. Besides the presence of LDH covering the electrode surface, other components are observed in this case (see Fig. 9D). The EDS analysis revealed that the detected particles had lower contents of Fe, Mg, and Al of about 17.05%, 7.29% and 3.52%, respectively, but a higher content of S element of 5.84% compared to the surface. It should be noted that the organic molecules released can adsorb onto metal surfaces and form coordination bonds based on the lone pair electrons of nitrogen and sulfur atoms in BTSA molecules.[19,55] Thus, we postulated the presence of complex products, which formed from the reaction between BTSA released and ferrous ions, leading to the formation of insoluble products on the steel surface.

The findings from SEM/EDS analysis supported the results of the study on the corrosion inhibition efficiency of LDH-BTSA, as observed in the electrochemical measurements. The release of BTSA and its interaction with the steel surfaces resulted in the formation of insoluble species, which combined with the deposition of a lamellar structure of LDH onto the steel substrates. This formed a barrier that effectively blocked the invasion of aggressive Cl^- anions, resulting in high levels of protection.

4. Conclusions

In conclusion, we reported a simple and efficient approach to preparing uniform LDH nanosheets. A high-speed homogenizer was applied to disperse the agglomerated LDH precursors into homogeneous smaller pieces, thereby promoting individual crystallite growth and limiting the LDH nanosheet stacking. Then, the uniform nanosheets can be tailored during the Ostwald ripening *via* the hydrothermal treatment process. The resulting nanosheets exhibited circular nanoplate morphology with a well-distributed particle size ranging from 50 to 250 nm and an average thickness of about 2–3 nm. The LDH-BTSA nanocontainers were successfully synthesized through the anion exchange of LDH nanosheets with organic inhibitor anions. The amount of BTSA intercalated in the LDH was reached at about 38 wt% after 24 h of anion exchange. LDH-BTSA can trap aggressive anions and release a large number of inhibitors during exposure to the corrosive medium. Thus, it revealed the high inhibition efficiency on the steel electrode of 90.3% at 2 h of immersion in a 0.1 M NaCl solution. The surface analysis shows that the barrier films were formed on electrode surfaces by the deposition of the lamellar structure of LDHs and the insoluble products of BTSA with ferrous ions, which can work as protective layers to protect metal surfaces from aggressive anions. This work demonstrated that the LDH nanosheets can be utilized as efficient nanocontainers for organic inhibitor loading and anti-corrosion application.

Author contributions

Minh Vuong, Phan: conceptualization, methodology, project administration, writing – review & editing; Thi Kim Thoa, Tran: investigation, validation, writing – original draft; Quynh Nhu, Pham: formal analysis, investigation, validation; Thi Hong No, Nguyen; Minh Ty, Nguyen: investigation, formal analysis; Manh Huy, Do: methodology, validation; Thanh Thao, Phan; Thi Xuan Hang, To: supervision, conceptualization, writing – review & editing.

Conflicts of interest

The authors declare that they have no known competing financial interests or personal relationships that could have appeared to influence the work reported in this paper.

Acknowledgements

This research is funded by the Vietnam Academy of Science and Technology under grant number ĐLTE00.05/21-22. The authors thank the Institute of Chemical Technology for their support facilities.

References

1 D. A. Leal, A. Kuznetsova, G. M. Silva, J. Tedim, F. Wypych and C. E. B. Marino, Layered materials as nanocontainers for active corrosion protection: a brief review, *Appl. Clay Sci.*, 2022, **225**, 106537.
2 Y. Zhang, H. Xu and S. Lu, Preparation and application of layered double hydroxide nanosheets, *RSC Adv.*, 2021, **11**(39), 24254–24281.
3 C. Ren, M. Zhou, Z. Liu, L. Liang, X. Li, X. Lu, H. Wang, J. Ji, L. Peng and G. Hou, Enhanced fluoride uptake by layered double hydroxides under alkaline conditions: solid-state NMR evidence of the role of surface> MgOH sites, *Environ. Sci. Technol.*, 2021, **55**(22), 15082–15089.
4 M. Duan, S. Liu, Q. Jiang, X. Guo, J. Zhang and S. Xiong, Recent progress on preparation and applications of layered double hydroxides, *Chin. Chem. Lett.*, 2022, **33**(10), 4428–4436.
5 W. Gou, X. Wang, M. Zhu, D.-X. Guan, X. Mo, H. Wang and W. Li, Long-range and short-range structures of multimetallic layered double hydroxides, *J. Phys. Chem. C*, 2022, **126**(11), 5311–5322.
6 S. Miyata, The syntheses of hydrotalcite-like compounds and their structures and physico-chemical properties-I: the systems Mg^{2+}-Al^{3+}-NO_3^-, Mg^{2+}-Al^{3+}-Cl^-, Mg^{2+}-Al^{3+}-ClO_4^-, Ni^{2+}-Al^{3+}-Cl^- and Zn^{2+}-Al^{3+}-Cl^-, *Clays Clay Miner.*, 1975, **23**, 369–375.
7 F. Cavani, F. Trifiro and A. Vaccari, Hydrotalcite-type anionic clays: preparation, properties and applications, *Catal. Today*, 1991, **11**(2), 173–301.

8 M. Ogawa and H. Kaiho, Homogeneous precipitation of uniform hydrotalcite particles, *Langmuir*, 2002, **18**(11), 4240–4242.
9 Y. Wang, L. Yang, X. Peng and Z. Jin, High catalytic activity over novel Mg–Fe/Ti layered double hydroxides (LDHs) for polycarbonate diols (PCDLs): synthesis, mechanism and application, *RSC Adv.*, 2017, **7**(56), 35181–35190.
10 Q. Wang, H. H. Tay, Z. Guo, L. Chen, Y. Liu, J. Chang, Z. Zhong, J. Luo and A. Borgna, Morphology and composition controllable synthesis of Mg–Al–CO_3 hydrotalcites by tuning the synthesis pH and the CO_2 capture capacity, *Appl. Clay Sci.*, 2012, **55**, 18–26.
11 S.-D. Jiang, Z.-M. Bai, G. Tang, L. Song, A. A. Stec, T. R. Hull, Y. Hu and W.-Z. Hu, Synthesis of mesoporous silica@ Co–Al layered double hydroxide spheres: layer-by-layer method and their effects on the flame retardancy of epoxy resins, *ACS Appl. Mater. Interfaces*, 2014, **6**(16), 14076–14086.
12 B. Chen, Q. Sun, D. Wang, X. F. Zeng, J. X. Wang and J. F. Chen, High-gravity-assisted synthesis of surfactant-free transparent dispersions of monodispersed MgAl-LDH nanoparticles, *Ind. Eng. Chem. Res.*, 2020, **59**(7), 2960–2967.
13 Z. Chen, N. Scharnagl, M. L. Zheludkevich, H. Ying and W. Yang, Micro/nanocontainer-based intelligent coatings: synthesis, performance and applications–A review, *Chem. Eng. J.*, 2023, **451**, 138582.
14 D. Tichit, G. Layrac and C. Gérardin, Synthesis of layered double hydroxides through continuous flow processes: a review, *Chem. Eng. J.*, 2019, **369**, 302–332.
15 T. Kameda, D. Ikeda, S. Kumagai, Y. Saito and T. Yoshioka, Synthesis of layered double hydroxide nanosheets in an aqueous solvent and their Ni^{2+} uptake characteristics, *Appl. Clay Sci.*, 2021, **200**, 105911.
16 X. Pang, M. Sun, X. Ma and W. Hou, Synthesis of layered double hydroxide nanosheets by coprecipitation using a T-type microchannel reactor, *J. Solid State Chem.*, 2014, **210**(1), 111–115.
17 Z. Ding, J. Li, B. Zhang and Y. Luo, Rapid and high-concentration exfoliation of montmorillonite into high-quality and mono-layered nanosheets, *Nanoscale*, 2020, **12**(32), 17083–17092.
18 Q. Wang and D. O'Hare, Recent advances in the synthesis and application of layered double hydroxide (LDH) nanosheets, *Chem. Rev.*, 2012, **112**(7), 4124–4155.
19 A. Liu, H. Tian, W. Li, W. Wang, X. Gao, P. Han and R. Ding, Delamination and self-assembly of layered double hydroxides for enhanced loading capacity and corrosion protection performance, *Appl. Surf. Sci.*, 2018, **462**, 175–186.
20 A. Liu, X. Ju, H. Tian, H. Yang and W. Li, Direct synthesis of layered double hydroxides monolayer nanosheets for co-assembly of nanobrick wall hybrid film with excellent corrosion resistance, *Appl. Surf. Sci.*, 2019, **493**, 239–249.
21 J. Yu, Q. Wang, D. O'Hare and L. Sun, Preparation of two dimensional layered double hydroxide nanosheets and their applications, *Chem. Soc. Rev.*, 2017, **46**(19), 5950–5974.
22 W. Yu, N. Du and W. Hou, Solvothermal synthesis of carbonate-type layered double hydroxide monolayer nanosheets: solvent selection based on characteristic parameter matching criterion, *J. Colloid Interface Sci.*, 2021, **587**, 324–333.
23 N. P. Funnell, Q. Wang, L. Connor, M. G. Tucker, D. O'Hare and A. L. Goodwin, Structural characterisation of a layered double hydroxide nanosheet, *Nanoscale*, 2014, **6**(14), 8032–8036.
24 L. Ma, Y. Qiang and W. Zhao, Designing novel organic inhibitor loaded MgAl-LDHs nanocontainer for enhanced corrosion resistance, *Chem. Eng. J.*, 2021, **408**, 127367.
25 C. Jaubertie, M. Holgado, M. San Román and V. Rives, Structural characterization and delamination of lactate-intercalated Zn,Al-layered double hydroxides, *Chem. Mater.*, 2006, **18**(13), 3114–3121.
26 S. Bai, T. Li, H. Wang, L. Tan, Y. Zhao and Y.-F. Song, Scale-up synthesis of monolayer layered double hydroxide nanosheets via separate nucleation and aging steps method for efficient CO_2 photoreduction, *Chem. Eng. J.*, 2021, **419**, 129390.
27 Y. Yan, Q. Liu, J. Wang, J. Wei, Z. Gao, T. Mann, Z. Li, Y. He, M. Zhang and L. Liu, Single-step synthesis of layered double hydroxides ultrathin nanosheets, *J. Colloid Interface Sci.*, 2012, **371**(1), 15–19.
28 J. Yu, B. R. Martin, A. Clearfield, Z. Luo and L. Sun, One-step direct synthesis of layered double hydroxide single-layer nanosheets, *Nanoscale*, 2015, **7**(21), 9448–9451.
29 L. Li, Z. Gu, W. Gu and Z. Xu, Direct synthesis of layered double hydroxide nanosheets for efficient siRNA delivery, *RSC Adv.*, 2016, **6**(98), 95518–95526.
30 Q. Qin, Y. Hu, J. Wang, Y. Yang, T. Lei, Z. Cui, S. Guo and S. Qin, Preparation of water-dispersed monolayer LDH nanosheets by SMA intercalation to hinder the restacking upon redispersion in water, *Nanoscale Adv.*, 2023, **5**(11), 2873–2878.
31 T. Hibino and M. Kobayashi, Delamination of layered double hydroxides in water, *J. Mater. Chem.*, 2005, **15**(6), 653–656.
32 Y. Zhao, F. Li, R. Zhang, D. G. Evans and X. Duan, Preparation of layered double-hydroxide nanomaterials with a uniform crystallite size using a new method involving separate nucleation and aging steps, *Chem. Mater.*, 2002, **14**(10), 4286–4291.
33 Z. P. Xu, G. S. Stevenson, C. Q. Lu, G. Q. Lu, P. F. Bartlett and P. P. Gray, Stable suspension of layered double hydroxide nanoparticles in aqueous solution, *J. Am. Chem. Soc.*, 2006, **128**(1), 36–37.
34 X. Sun and S. K. Dey, Insights into the synthesis of layered double hydroxide (LDH) nanoparticles: part 2. Formation mechanisms of LDH, *J. Colloid Interface Sci.*, 2015, **458**, 160–168.
35 A. Eliseev, A. Lukashin, A. Vertegel, V. Tarasov and Y. D. Tret'yakov, A study of crystallization of Mg–Al double hydroxides, *Dokl. Chem.*, 2002, 339–343.
36 Y. Zheng and Y. Chen, Preparation of polypropylene/Mg–Al layered double hydroxides nanocomposites through wet pan-milling: formation of a second-staging structure in LDHs intercalates, *RSC Adv.*, 2017, **7**(3), 1520–1530.

37 A. Yadav, M. Pal and R. L. Goswamee, Biocompatible nanocomposite of carboxymethyl cellulose and functionalized carbon–norfloxacin intercalated layered double hydroxides, *Carbohydr. Polym.*, 2018, **186**, 282–289.
38 D. Vieira, D. Sokol, A. Smalenskaite, A. Kareiva, M. Ferreira, J. Vieira and A. Salak, Cast iron corrosion protection with chemically modified MgAl layered double hydroxides synthesized using a novel approach, *Surf. Coat. Technol.*, 2019, **375**, 158–163.
39 E. Bernard, W. J. Zucha, B. Lothenbach and U. Mäder, Stability of hydrotalcite (Mg-Al layered double hydroxide) in presence of different anions, *Cem. Concr. Res.*, 2022, **152**, 106674.
40 N. Bhojaraj, J. Arulraj, M. R. Kolinjavadi and M. Rajamathi, Solvent-mediated and mechanochemical methods for anion exchange of carbonate from layered double hydroxides using ammonium salts, *ACS Omega*, 2019, **4**(22), 20072–20079.
41 M. Ulibarri, I. Pavlovic, C. Barriga, M. Hermosın and J. Cornejo, Adsorption of anionic species on hydrotalcite-like compounds: effect of interlayer anion and crystallinity, *Appl. Clay Sci.*, 2001, **18**(1–2), 17–27.
42 N. Fajrina, N. Yusof, A. Ismail, J. Jaafar, F. Aziz, W. Salleh and N. Nordin, MgAl-CO_3 layered double hydroxide as potential filler in substrate layer of composite membrane for enhanced carbon dioxide separation, *J. Environ. Chem. Eng.*, 2021, **9**(5), 106164.
43 D. T. Nguyen, H. T. X. To, J. Gervasi, Y. Paint, M. Gonon and M.-G. Olivier, Corrosion inhibition of carbon steel by hydrotalcites modified with different organic carboxylic acids for organic coatings, *Prog. Org. Coat.*, 2018, **124**, 256–266.
44 T. T. X. Hang, T. A. Truc, N. T. Duong, P. G. Vu and T. Hoang, Preparation and characterization of nanocontainers of corrosion inhibitor based on layered double hydroxides, *Appl. Clay Sci.*, 2012, **67**, 18–25.
45 T. T. X. Hang, T. A. Truc, N. T. Duong, N. Pébère and M.-G. Olivier, Layered double hydroxides as containers of inhibitors in organic coatings for corrosion protection of carbon steel, *Prog. Org. Coat.*, 2012, **74**(2), 343–348.
46 S. Poznyak, J. Tedim, L. Rodrigues, A. Salak, M. Zheludkevich, L. Dick and M. Ferreira, Novel inorganic host layered double hydroxides intercalated with guest organic inhibitors for anticorrosion applications, *ACS Appl. Mater. Interfaces*, 2009, **1**(10), 2353–2362.
47 T. A. Truc, T. T. Thuy, V. K. Oanh, T. T. X. Hang, A. S. Nguyen, N. Caussé and N. Pébère, 8-hydroxyquinoline-modified clay incorporated in an epoxy coating for the corrosion protection of carbon steel, *Surf. Interfaces*, 2019, **14**, 26–33.
48 T. D. Nguyen, A. S. Nguyen, B. A. Tran, K. O. Vu, T. T. Phan, N. Scharnagl, M. L. Zheludkevich and T. X. H. To, Molybdate intercalated hydrotalcite/graphene oxide composite as corrosion inhibitor for carbon steel, *Surf. Coat. Technol.*, 2020, **399**, 126165.
49 M. Tabish, G. Yasin, M. J. Anjum, M. U. Malik, J. Zhao, Q. Yang, S. Manzoor, H. Murtaza and W. Q. Khan, Reviewing the current status of layered double hydroxide-based smart nanocontainers for corrosion inhibiting applications, *J. Mater. Res. Technol.*, 2021, **10**, 390–421.
50 T. D. Nguyen, B. A. Tran, K. O. Vu, A. S. Nguyen, A. T. Trinh, G. V. Pham, T. X. H. To, M. V. Phan and T. T. Phan, Corrosion protection of carbon steel using hydrotalcite/graphene oxide nanohybrid, *J. Coat. Technol. Res.*, 2019, **16**(2), 585–595.
51 A. Braig, in *Proceeding of the Symposium on Advance in Corrosion Protection by Organic Coatings III*, ed. I. Sekine, Electrochemical Society, 1998, pp. 18–31.
52 F. Calegari, B. C. da Silva, J. Tedim, M. G. Ferreira, M. A. Berton and C. E. Marino, Benzotriazole encapsulation in spray-dried carboxymethylcellulose microspheres for active corrosion protection of carbon steel, *Prog. Org. Coat.*, 2020, **138**, 105329.
53 E. Alibakhshi, E. Ghasemi, M. Mahdavian and B. Ramezanzadeh, A comparative study on corrosion inhibitive effect of nitrate and phosphate intercalated Zn-Al-layered double hydroxides (LDHs) nanocontainers incorporated into a hybrid silane layer and their effect on cathodic delamination of epoxy topcoat, *Corros. Sci.*, 2017, **115**, 159–174.
54 J. Rodriguez, E. Bollen, T. Nguyen, A. Portier, Y. Paint and M.-G. Olivier, Incorporation of layered double hydroxides modified with benzotriazole into an epoxy resin for the corrosion protection of Zn-Mg coated steel, *Prog. Org. Coat.*, 2020, **149**, 105894.
55 C. Verma, E. E. Ebenso and M. Quraishi, Corrosion inhibitors for ferrous and non-ferrous metals and alloys in ionic sodium chloride solutions: a review, *J. Mol. Liq.*, 2017, **248**, 927–942.